

RU663

FEB 20 1964

APPENDIX IV

MESOSCALE NOWCASTING OF SEA ICE MOVEMENT
THROUGH THE BERING STRAIT
WITH A DESCRIPTION OF MAJOR DRIVING FORCES

by

T.L. Kozo
W.J. Stringer
L.J. Torgerson

MESOSCALE NOWCASTING OF SEA ICE MOVEMENT

THROUGH THE BERING STRAIT

WITH A DESCRIPTION OF MAJOR DRIVING FORCES

THOMAS L. KOZO

Occidental College, VANTUNA Research Group

Los Angeles, CA 90041

WILLIAM J. STRINGER

University of Alaska, Geophysical Institute

Fairbanks, AK 99701

LENORA J. TORGERSON

University of Alaska, Geophysical Institute

Fairbanks, AK 99701

ABSTRACT

Surface **atmospheric** pressure data from a triangular station network surrounding the Bering Strait are used to calculate hypothetical **geostrophic** wind **velocities**. Net daily Strait sea ice movement is derived from visible **and** infrared NOAA satellite imagery for November through May, **1974 to 1984**. **These** historical ice-motion data and network wind-velocity data are used to develop an empirical 12-h advance forecast (**nowcast**) sea ice movement model with all-weather capabilities, A necessary outgrowth of this study has **been** **the** identification and classification of **three** modes of ice movement **and** two modes of ice immobilization according to their major driving forces. The first ice-movement mode is from the **Chukchi** to the Bering Sea requiring a **minimum northeasterly** geostrophic wind of 12 ms^{-1} . The second and third **modes** represent ice movement from the Bering to the **Chukchi** Sea. Mode two is driven by a preexisting north-flowing ocean current that offsets weak winds from the northeast. Mode three is large movement due to a combination of southwesterly winds and north-flowing ocean **current**. The first immobilization mode (maximum duration one week) is an apparent balance between northerly wind stress, current stress from the south, and internal ice stresses. The second immobilization mode (least common) is due to double, solid sea ice arches forming across the Strait. These arches remained intact under strong northeasterly geostrophic winds ($20-26 \text{ ms}^{-1}$) and can last up to four weeks.

1. Introduction

Both northward and southward sea ice movement through the Bering Strait can be hazardous to future oil development in the northern Bering Sea (Fig. 1, see for most place names in this paper). This wind- and current-dependent movement can be extensive from November to May and is connected to dynamic interactions with sea ice in the vicinities of St. Lawrence Island (Shapiro and Burns, 1975a; Sodhi, 1977) and Norton Sound (Stringer and Hufford, 1982). Southward ice movement below the Strait is related to westward ice movement (Fig. 2, bottom) out of the Sound while northward ice movement toward the Bering Strait is related to eastward ice movement (Fig. 3, bottom] into the Sound (Stringer and Hufford, 1982). Computerized pattern-recognition techniques (Hufford and Scheidt, 1983) show that atmospheric pressure patterns most often associated with these two cases are those in the top portions of Fig. 2 and Fig. 3 respectively. Note that northward ice movement into and through the Strait is associated with a type of atmospheric relaxation and a weak pressure gradient in the Strait area (Fig. 3, top).

There have been numerous papers since the seventies relating sea ice motion and oceanic transport in the Bering Strait to some type of meteorological forcing. Shapiro and Burns (1975b) used sequential Landsat (National Aeronautics and Space Administration, NASA) and DAPP (U.S. Air Force) imagery to construct displacement vectors for ice floes moving through the Strait. A relationship between southward ice movement and northerly surface winds at Cape Wales on the western tip of the Seward Peninsula was demonstrated. Analyses of National Oceanic and Atmospheric Administration (NOAA) surface synoptic weather charts explained episodes of alternating

south and north sea ice motion (Ray and Dupre, 1981) and several extensive southward movements (Kovacs et al., 1982). Reimer et al. (1979) studied similar extensive southward ice movements, called "breakout," that were preceded by sea ice fracture. They modeled the Strait as a **two-dimensional chute, and the necessary load** required to fracture and push ice was computed. A two-point atmospheric pressure difference from Cape Schmidt (Siberia) to Nome (Alaska) exceeding 20 mb was related to these events in the winters of 1975 and 1976. Coachman and Aagaard (1981) also showed that two-point atmospheric pressure differences (i.e., Provideniya to Nome) were correlated with oceanic transport directions. However, none of these differences were true pressure gradients, requiring a minimum of three simultaneous surface pressures. True pressure gradients are both proportional and perpendicular to the geostrophic wind velocity, which in turn can be converted to wind stress. For example, the 20 mb pressure difference mentioned above amounts to a geostrophic wind of approximately 15 ms^{-1} from 40° only if the isobars are perpendicular to a line joining the reporting stations. It is shown in this paper, on examination of an extensive data base, that ice moves south through the Strait for a suite of geostrophic wind velocities that often have Cape Schmidt to Nome pressure differences less than 20 mb. Aagaard et al. (1985) add evidence for the feasibility of predicting ice movement from pressure-field wind calculations. They combined National Weather Service (NWS) synoptic pressure data with Fleet Numerical Oceanography Center (FNOO) techniques to predict theoretical surface winds for the Strait. A high correlation of oceanic transport to the meridional wind component in two different current-data collection years was demonstrated. Unfortunately, this last technique assumes a uniform surface wind field within 300 km of the Strait. This is highly improbable due to a tendency for mesoscale orographic

effects to propagate offshore (Kozo, 1984). Examples of synoptic pressure fields and actual surface winds can be seen in Section 4.

The main objective of this study is to create a nomogram for all-western, short-term prediction or **nowcasting** (Browning? 1982) of **sea ice** movement through **the** Bering Strait from **mesoscale** network computed **geostrophic** wind velocities. Successful use of **mesoscale** networks with **their** increased resolution and predictive capabilities over synoptic networks **in the** Arctic has been documented by Kozo (1980, 1984). The wind velocities are derived **in** a straightforward manner using an atmospheric pressure network encompassing the Bering Strait with three World Meteorological Organization (WMO) reporting stations: **Uelen** (U, Siberia), **Provideniya** (P, Siberia), and **Nome** (N, Alaska). The sea ice motion data were compiled from 11 years of daily visible and infrared NOAA 3-8 satellite image transparencies.

As a by-product of this study, three modes of ice movement and two modes of ice immobilization in the **Strait** have been identified **and** classified according to major driving forces.

2. Study Area

The Bering Strait's oceanic cross **section** is roughly 85 km x 50 m and its annual average transport is ~ 0.6 Sv (Aagaard et al., 1985) to the north, attributed to higher sea level in the Bering Sea than in the Arctic Ocean (Coachman and Aagaard, 1981; Stigebrandt, 1984). This relatively small **annual northward** transport would be five times greater if not for wind-induced flow reversals to the south occurring two to three times per month and lasting six to twelve days (Kovacs and Sodhi, 1981). **Daily** mean transport can reach 3.1 Sv to the north (Coachman and Aagaard, 1981), which

implies currents up to 70 cm s^{-1} , given the above cross-sectional area.

Current velocities of this magnitude are indications that oceanic flow driven north or south tends to be funneled (see Fig. 1) and accelerated on entering the Strait (Coachman et al., 1975).

The same funneling applies to arctic winds in the Strait, which tend to flow-around rather than over topography (Kozo, 1984). The Chukchi and Seward Peninsulas have small mountain ranges setting north to east and north to west, respectively. (Fig. 1). Their elevations are at least equal to 600 m, which is sufficient to redirect and accelerate air flow during winter conditions (Dickey, 1961).

During this study, it became apparent that ice moved north or south through the Strait as if on a "conveyor belt" (Kozo and Tucker, 1974) for a suite of computed wind-velocity vectors. Therefore, relating ice movement thresholds to a wind-velocity component parallel to an assumed Strait axis orientation would simplify development of a prediction nomogram. There are several choices of axis orientation. For this paper, the Strait axis orientation was chosen to be perpendicular to the line from Cape Schmidt to Nome or 40°E from the north. In this way, comparisons can be made with earlier work where a positive pressure difference (20 mb) between Cape Schmidt and Nome signaled ice breakout into the Bering Sea (Reimer et al., 1979) .

3. Data

a. Surface atmospheric pressure and temperature

Barometric pressure data, reduced to sea level, and temperature data taken simultaneously from Uelen ($66^\circ 10' \text{N}$, $169^\circ 50' \text{W}$), Bukhta Provideniya

(64°26'N, 173°14'W), and Nome (64°30'N, 165°24'W) are used to compute a geostrophic wind for the Bering Strait. The accuracies of these pressure and temperature data from Nome, a first-order weather station, are better than ± 0.25 mb and $\pm 1^\circ\text{C}$, respectively. The two Russian stations are part of a global network that transmits real-time data to the National Meteorological Center (NMC) and are assumed to be within these limits also.

b. Geostrophic wind data

These data were computed from the pressure and temperature data provided by the three above weather stations. The atmospheric flow was assumed to be in geostrophic balance (1):

$$f(\mathbf{k} \times \mathbf{V}_G) + \frac{\nabla P}{\rho} = 0 \quad (1)$$

The first term is the Coriolis force, and the second is the pressure gradient force. f is the Coriolis parameter ($1.321 \times 10^{-4} \text{ sec}^{-1}$ at 65°N), \mathbf{k} is the vertical unit vector, \mathbf{V}_G is the geostrophic velocity vector, ∇P is the gradient of the atmospheric pressure, and ρ is the air density. Using station grid (Fig. 1), pressure can be represented as a function of latitude (Y) and longitude (x) on a plane surface:

$$\begin{aligned} P_N(x,y) &= ax_N + by_N + c \\ P_U(x,y) &= ax_U + by_U + c \\ P_P(x,y) &= ax_P + by_P + c \end{aligned} \quad (2)$$

The subscripts N, U, and P denote Nome, Uelen, and Provideniya, respectively. Pressure (1?) data and relative positions of each station are known on an x,y grid. Cramer's rule can be applied to (2) to solve for unknowns a, b, and c. Since $\partial P/\partial x = a$ and $\partial P/\partial y = b$, the pressure gradient (∇P) can be computed. The geostrophic velocity (V_G) can now be calculated from (1) since f is known and ρ for dry air can be estimated from station temperatures.

Station errors of $\pm 1^\circ\text{C}$ (see above) in temperature can cause errors of 0.34% in the velocity magnitude since they affect p estimates. Station errors in pressure of ± 0.25 mb can cause maximum speed errors $\pm 1.4\text{ms}^{-1}$ and direction errors greater than $\pm 15^\circ$ for wind speeds below 3ms^{-1} . An example of this would be using "true" surface pressures of 1020 mb, 1021.05 mb, and 1020 mb at Provideniya, Uelen, and Nome, respectively, in (1) and (2). A V_G of 3ms^{-1} from 88.6° is obtained. Changing these "true" surface pressures by 0.25 mb to 1019.75 mb, 1020.8 mb, and 1020.25 mb, respectively, results in a V_G of 2.5 from 105.2° or a direction error of 16.6° . Therefore, at wind speed $\leq 3\text{ms}^{-1}$, wind directions should not be considered significant.

c. Satellite imagery

The ice-motion data came primarily from visible and infrared NOAA 3-8 VHRR (Very High Resolution Radiometer) satellite imagery. The infrared imagery was utilized mainly during December, January, and February when daylight was minimal. To minimize errors due to the earth's curvature, the scale was taken from the closest land mass. The net 24-h ice motion was measured directly by tracking identifiable floes or indirectly by measuring the change in ice edge location south or north of the Diomedes Islands. A minimum of two days' imagery is necessary to document a displacement with an error estimated at ± 5 km.

During the ice-covered months (November through May) from 1974 to 1984, nearly 40% of the total observation days were obscured by cloud-related undercast. However, the technique outlined below based on the remaining 60% of the data, if representative, will be an all-weather, undercast-independent predictive tool.

4. Results with Discussion

a. Sea ice injections

Satellite imagery (1974 to 1984) has shown many five- to seven--day episodes of extensive south and north sea ice movement analogous to ice injections through the Strait. There have been 39 cases of southward injections into the Bering Sea and 19 cases of northward injections into the Chukchi Sea. The total ice input for each of these events was approximately equal to or greater than the areal extent of St. Lawrence Island (SLI). Of the 39 southward cases, 17 had an input more than twice the area of SLI. For the 19 northward cases, only seven occurred with an input of double SLI's area.

b. Constructing the sea ice movement prediction nomogram

Net daily sea ice movements derived from satellite imagery have been examined and compared to simultaneous mesoscale atmospheric pressure network (MAPN) computed V_G 's to produce an empirical nowcast nomogram (Fig. 4). No estimates of turning angle between V_G and the wind velocity at the surface (V_S) were made, due to orographic effects (channeling and blockage). Table 1

lists some of the events used in the nomogram construction and classifies them according to mode (major driving force) and zone (net movement and direction). The Greek and Latin letters from Table 1 are positioned in Fig. 4 to represent a MAPN-computed V_G (direction [from] and speed as independent variables). The directions indicated are those from which the wind is blowing. The small center circle represents V_G 's with speeds less than 3 ms^{-1} . Due to measurement errors and the minimal effects on ice motion at these low wind speeds, V_G 's within this circle should be considered as approximately zero winds. V_{40} (see Table 1, definition B for sign) represents the V_G component parallel to the assumed Strait axis, 40° from north. This axis is indicated by ice movement direction arrows that meet in the Zero Net Ice Motion Zone, one of five zones defined by wind-speed ranges along the V_{40} axis. These nomogram zones are used to characterize three ice-motion modes and two ice-immobilization modes in the Strait. Four predictable modes are described below. The fifth mode, though not yet predictable, was a discovery of this procedure and will be discussed later.

Mode 1 contains two zones of wind-forced sea ice movement into the Bering Sea which initially must offset a northward-flowing ocean current (Aagaard et al., 1985; Stigebrandt, 1984). The threshold for southward movement is a V_{4i} , exceeding 11.5 ms^{-1} . The bounds in 40° or each one are shown in Table 1 and Fig. 4. The $>20 \text{ km (day)}^{-1}$ Zone conditions would push an amount of ice into the Bering Sea sea approximately equal to double the area of St. Lawrence Island for five days. Examples of Mode 1 occurred 11, 20, and 27 December 1976, during total ice cover when the Bering Strait ocean current at 10 m from the bottom switched from north to south (Coachman and Aagaard, 1981). The average MAPN-computed V_G during these three cases was 29 ms^{-1} from 61° (ψ , Fig. 4). The 27 December 1976 event, with clear satellite imagery, showed net southward Strait ice movement of 23 km.

Mode 2 includes **only one** nomogram zone. Sea ice movement is northward into **the Chukchi Sea**, and this mode is ocean current dominated with minor opposing wind influence. The northward movement represented by the ICE INTO CHUKCHI ZONE with $0 \text{ ms}^{-1} \leq V_{40} \leq 7.5 \text{ ms}^{-1}$, is due to a preexisting northward-flowing ocean **current** that overpowers **the weak opposing wind**. A V_S approximately 60% of V_{40} (7.5 ms^{-1}) is 4.5 ms^{-1} or the WMO equivalent of a **gentle breeze**. Nevertheless, the net northward sea ice movement is reduced to less than 20 km (day)^{-1} . This current appears to be a combination of residual contributions (Liu and Leendertse, 1985) from the Bering Sea tide and a permanent downward sea level slope (Coachman and Aagaard, 1981) from the Bering toward the **Chukchi** of steric origin (Stigebrandt, 1984).

Mode 3 includes the ICE INTO CHUKCHI $>20 \text{ km (day)}^{-1}$ ZONE T with $V_{40} \leq 0$. The wind and water stress are in the same direction. At wind speeds less than 5 ms^{-1} the current provides the major force, **while** at wind speeds greater than 5 ms^{-1} the current and wind act together. The low wind-speed periods correspond to the example shown in Fig. 3. All wind speeds in this mode produce northward ice motion adjacent to Norton Sound and Chukchi sea ice injections of double the SLI area in five days. However, higher wind-speed events ($>5 \text{ ms}^{-1}$) have sometimes produced less net movement than the low-wind-speed or current-dominated events. The latter cases represent a more localized Strait-area current drag on the sea ice canopy, while the former cases are a combination of the localized current drag and a large area wind stress pushing the entire sea ice canopy in the northern Bering Sea. The nomogram breakdown of the net daily sea ice motion into 20-km slots despite satellite imagery **displacement** accuracy of $\pm 5 \text{ km}$ is a result of this phenomenon. This indicates that opposing internal and boundary ice stresses may play an important role at higher wind speeds. "

Mode 4 is one of zero net ice movement, usually lasting less than one week, with $7.5 \text{ ms}^{-1} < V_{40} < 11.5 \text{ ms}^{-1}$. The primary force balance in the Strait area is between the wind stress pushing ice south and the water stress pushing ice north. Again, internal ice stresses and shore-fast ice (boundary) effects must play a role, but they are beyond the scope of this study. The relative magnitudes of the opposing surface wind stress (τ_a) and water stress (τ_w) are quite comparable and add credibility to the nomogram design (see Appendix A).

c. Using the nomogram

The nomogram users would follow a simple procedure provided that they have access to weather-data transmissions similar to that of NMC. Simultaneous surface-pressure and temperature data from Uelen, Provideniya, and Nome for 00 and 1200 GMT should be available to the user less than three hours after recording at the respective stations. These data (P_N, P_U, P_P) can be combined with (2) to solve for VP. Air density (ρ) is approximated using a three-station average temperature and the equation of state for dry air, $\rho = P(RT)^{-1}$. P is the standard sea-level atmospheric pressure (1013.3 mb), R is the gas constant, and T is the absolute temperature. The solution for VP, ρ and V_G can be obtained from (1). The V_G for 00 and 1200 GMT are combined to obtain an average velocity (\bar{V}_G). Once \bar{V}_G is known, the two necessary independent variables speed (radius vector) and direction (vectorial angle), can be plotted on polar-coordinate graph paper with the nomogram's five wind-speed zones and V_{40} axis superimposed. For example, using data from Fig. 5, $P_N = 999.4 \text{ mb}$, $P_P = 1008.0 \text{ mb}$, $P_U = 1011.3 \text{ mb}$, and an average temperature of -5°C (not shown), $V_G = 23 \text{ ms}^{-1}$ from 56.8° (see arrow).

Plotting this value (X) on Fig. 6 (bottom) and drawing a perpendicular from the τ_{40} axis to X predicts net ice movement $>20 \text{ km (day)}^{-1}$ to the south. The net ice movement obtained from satellite imagery was 45 km south.

d. Testing the nomogram technique

1) Advantages of the MAPN-computed V_G over other techniques

Figure 7 shows the advantage of the MAPN for predicting Bering Strait ice movement over that of the NMC surface pressure analysis. The NMC surface synoptic analysis for 21 April 1982, 1200 Greenwich Mean Time (GMT) gives no indication of a strong southwesterly wind. In addition, the surface wind directions at Uelen (U), Provideniya (P), and Nome (N) are all different. The MAPN-calculated V_G was 12.4 ms^{-1} from 248° , which fits an observed net ice motion (satellite imagery) of 14 km north ($\pm 5 \text{ km}$) for the day.

Figure 8 demonstrates the MAPN advantage over both pattern recognition and NMC synoptic analysis. A type of "relaxed" atmospheric pressure field has existed for four days (Fig. 3, top), which denotes probable northward ice movement. However, the MAPN-calculated geostrophic wind velocity indicates that the "brakes" are being applied to northward sea ice movement. The 1200 GMT, 25 March 1978 V_G was 11.0 ms^{-1} from 75° , and the \bar{V}_G for the next 12-h period was 12.4 ms^{-1} from 68.4° . The net ice movement switched from north to 6 km south by 26 March. The surface winds surrounding the Strait appear to be less than 5 ms^{-1} , but their northerly direction may be a clue to the wind push direction (Fig. 8).

The effects of orography are striking, even with a well-defined surface pressure pattern as demonstrated on 5 April 1983 (Fig. 5). The large

variations in direction and speed of surface winds at P, U, and N are evidence that previous attempts (Reimer et al., 1979; Coachman et al., 1975) to correlate local winds with ice movement or ocean current direction in their vicinity met with limited success.

These above examples show also the dangers of using pure synoptic analyses to derive the surface wind field. In Aagaard et al. (1985) an error is made by assuming the surface wind field to be uniform within 300 km of the Strait.

2) NOAA satellite imagery

Figure 6 (bottom) represents the nomogram base chart as constructed from data in Fig. 4. A time period having 23 consecutive undercast-free days (6-28 April 1982) was chosen to test the accuracy of the MAPN and nomogram predictions. The numbers 6-28 are April dates and represent the \bar{V}_G positions combining the 00 and 1200 GMT V_G 's on those days. If the wind direction changed by more than 90° in 12 h, and/or the change reversed the direction of ice motion, no prediction would be made. If any of the three network stations failed to report at either the 00 or 1200 GMT time periods, then the closest available simultaneous time period was used for the \bar{V}_G . Figure 6 (top) shows the net sea ice movement in km derived from satellite imagery for the corresponding days. Allowing for the error bounds on the imagery (± 5 km) and the V_G (± 1.4 ms⁻¹), the nomogram technique failed in only two cases.

The first case was 12 April 1982 where a V_G of 14 ms^{-1} from 22° produced 36 km of actual southward ice movement instead of the <20 km south predicted. Here the wind direction was 180° from the last major northward push (8 April 1982) and only the second day of consistent V_G 's from the northeast. There was evidently ample room for sea ice advected south through the Strait from the Chukchi Sea without need for additional deformation. It must be noted that this observed tendency for enhanced sea ice motion after a 180° wind-direction reversal agrees with observations for the Beaufort Sea (Agerton and Kreider, 1979). They have shown that major sea ice movement conditions are a wind-speed threshold of 13 ms^{-1} and alternation of stress application direction by 180° .

The second case on 25 April 1982 had 16 km net northward sea ice movement shown on the satellite imagery. The MAPN V_G of 10.2 ms^{-1} from 31.4° predicted zero net motion (Fig. 6). There is no satisfactory explanation for this discrepancy. However, examination of the surface pressure charts for this day showed an unusually complex isobaric pattern. This pattern could produce a wind system capable of moving ice to the south in the Kotzebue Sound area (Fig. 1) and to the north in the northern Bering Sea. Indeed, satellite imagery showed that sea ice offshore from Cape Lizburne moved south during this same period.

In summary, there were two bad predictions out of 23, or 91% correct, and only one prediction erred in the ice movement direction. The nomogram can be overlaid on polar-coordinate graph paper and MAPN-computed V_G 's plotted very simply. The perpendicular to the V_{40} axis should give the predicted net sea ice movement.

3) Buoy drift data (Reynolds and Pease, 1984)

Data buoys implanted on ice floes in the winter of 1982 were tracked by satellite through use of a position transponder called an ARGOS Data Acquisition Platforms (ADAP), Model 901. Each ADAP platform position is received 8-12 times per day with an accuracy of 200 m in longitude and 100 m latitude. Table 2 presents the nomogram predictions versus various net buoy-drift distances (Reynolds and Pease, 1984). The buoy locations chosen were within the MAPN grid between 1° south and 0.5° north of the Strait, (Fig. 1). The net movement data from individual buoys on various ice floes are from a smaller and different data base than net ice movement taken from satellite imagery. However, future projects, using the high resolution all-weather buoy capabilities, might provide data for fine-tuning the nomogram technique. At least one buoy and sometimes three were in the Strait area from 3 February to 3 April 1982. In Table 2, net buoy displacement (X) to the north (N) or south (S) can be compared to the nomogram predictions (NP) for the given MAPN-computed average velocities (V_G). There was agreement in 33 out of 39 days for 82.5% correct predictions. One case, 12 February 1982, had V_G change direction from 256° (13 ms^{-1}) to 74° (18 in^{-1}) in 12 hours, which is a condition not covered in the nomogram construction. On 17, 18, and 27 February and 22 and 26 March, the predictions erred in net distance but not direction. The 29 and 30 March dates each had buoy movement (X) of 8 km north while the nomogram predicted (NP) zero net motion.

The above-mentioned cases on 22 and 29 March 1982 were probably not in geostrophic balance (1). Both showed the pressure field changing rapidly during the 00 to 1200 GMT time period at MAPN stations. Therefore, an

additional wind velocity component proportional to the barometric tendencies directed from high to low tendency isopleths (isallobars) existed. The mathematical expression for the wind component due to a changing pressure distribution, isallobaric component (V_I), is (Brunt, 1941):

$$V_I = \frac{-\dot{V}_P}{f^2 \rho} \quad (3)$$

where all terms are defined as in (1) and (o) represents the partial derivative with respect to time. Using (3), the 22 March 1982 MAPN V_G (see Table 2) would have neglected an opposing V_I of $\sim 2 \text{ ms}^{-1}$ from 145° . The 29 March 1982 MAPN V (see Table 2) would have an opposing V_I of $\sim 1.5 \text{ ms}^{-1}$ from 227° . The same days also had weather maps showing isobars with the radius of curvature less than 300 km (Kozo 1982). In these situations centrifugal force can not be neglected and must be added to the terms in (1) for a force balance (gradient flow). The 22 and 29 March dates were instances of cyclonic flow making V_G an overestimate of the true free stream wind speed (V_T). The expression (Holton, 1973) for V_T is:

$$\frac{V_T^2}{r} + fV_T - fV_G = 0 \quad (4)$$

where $r \equiv$ radius of curvature of the isobars. Using (4), the 22 March V_T is 15.9 ms^{-1} from 45° which if used in the nomogram would give a correct prediction of $<20 \text{ km S}$ (see Table 2). The March 19 V_T is 8.5 ms^{-1} from 049° , which combined with V_I above gives a correct prediction of $<20 \text{ km N}$ within the MAPN error bounds.

The present MAPN does not include isallobaric effects or gradient flow since a simple prediction procedure was examined first. These extra refinements can be built into the wind-velocity calculation and on application to the nomogram will increase the accuracy ~5%.

e. Implications for oceanic transport mechanisms

It must be noted that net sea ice movements instead of currents were measured coincident with the time period discussed below. These movements, in cases of weak synoptic winds, give an indication surface current velocities. The 00 GMT, 11 May 1984 NMC surface synoptic chart (Fig. 9) shows a weak high to the southwest of the Strait promoting slight off-shelf water movement in the Bering Sea. In addition, the atmospheric pressure field shows a 12 mb decrease from the southwestern Bering to the northeastern Chukchi Sea. Both effects would tend to make the sea level in the Bering lower than in the Arctic Ocean, promoting southward current flow. This synoptic condition on 11 May was within a period (4 May to 15 May) of relatively weak winds. The net sea ice movement on 11 May was 18 km (± 5 km) north and followed a day of almost no motion. This was evidence that northward current flow occurs without southwesterly wind forcing and meteorological conditions that would create a sea level slope down to the north. The same event also showed that this flow can occur without a sea level imbalance caused by relaxation of previous strong northerly winds (Coachman and Aagaard, 1981). The MAPN-calculated V_e (Fig. 9) was a low 2.6 ins^{-1} from 58.7° but, as stated in Section 3, speeds $< 3 \text{ ms}^{-1}$ can have direction error of more than 15° . The synoptic charts for the entire day showed no winds strong or persistent enough to produce the recorded ice

movement. This **event** took **place** under relaxed conditions (Fig. 3) **found to represent** northward ice movement.

O There is **ample** evidence that **local** sea level sloping downward **to the north**, southwesterly winds, **and** compensatory flow after a strong northerly wind are sufficient conditions for northward oceanic transport; however, this example shows that they are **not** necessary conditions for this type of transport. Two recent papers show other possible mechanisms. **Stigebrandt (1984)** combines experimental and theoretical considerations based on salinity differences between the Atlantic and Pacific (global scale) to show that the Bering is ~ 0.5 m higher than the Arctic Ocean. Liu and Leendertse (1985) show in a modeling paper that a residual current flowing northward through the Strait evolves from a combination **of** the tides and the density field (negligible in winter). Therefore, a mean northward transport can exist in the absence of any meteorologically related effects.

f. Solid, double sea ice arches (Mode 5)

The double sea ice arch represents the longer duration second mode of ice immobilization. This mode is rare in the Bering Strait since only five cases (a possible sixth was noted on Landsat Data for 5 April 1976) have been found in 11 years of sea ice satellite data. A photograph made from a satellite image (Fig. 10) taken 5 May 1980 shows the characteristic solid, double ice arch using the tip of the Chukchi Peninsula (X), the Diomede Islands, **and** the Seward Peninsula tip (W) as anchor points. Norton Sound is **totally** free of ice except for shore-fast sea ice on the southern side, Also, there is a large expanse of open water (OW) south of the Bering Strait

arches and south of St. Lawrence Island. Since the image chosen was taken 21 days after the arches formed, it appears that it was not cold enough for new ice formation and the presence of arches prevented resupply by old ice advection from the north. These arches are not the arched fractures seen in sea ice during failure modes (Sodhi, 1977; Reimer et al., 1979) but evidently represent strong impediments to southward sea ice movement (see Appendix B for details). As evidence of the lack of fractures in the ice canopy during the solid-arch phase, the above (14 April to 10 May 1980) period represented a halt in whale (Bowhead) migration through the Strait (Hufford, 1984, National Weather Service, Anchorage, pers. comm.).

The double arches were discovered indirectly through failure of the nomogram prediction system. In all double-arch cases, the nomogram with \bar{V}_G from the MAPN predicted greater than 20 km (day)⁻¹ of net ice movement into the Bering for at least 50% of the arch period. Figure 11 shows sample MAPN V_G 's plotted on the nomogram from three of the arch periods: 14 April to 10 May 1980, 26 February to 8 March 1984, and 22 March to 21 April 1984. The V_G 's enclosed by the dashed oval have $V_{40} > 17 \text{ ms}^{-1}$, predicting large net ice movement into the Bering Sea. There were several '40's as high as 26 's with no ice movement. In addition, the greater than 20 mb pressure difference ice breakout criterion (Reimer et al., 1979) from Cape Schmidt to Nome was exceeded at some time during all the double-arch periods.

5 . Summary and conclusions

The combination of MAPN-calculated V_G 's with the nomogram provides an all-weather Bering Strait sea ice movement nowcasting capability with an average accuracy of approximately 85%. The MAPN improvement over NMC

surface pressure analyses and pattern-recognition techniques **has been** demonstrated. This study, **though** meteorologically oriented, also has shed **light on** oceanographic phenomena. . The ocean currents, **in particular, in the** Strait area **are crucial to** the prediction scheme.

a. Sea ice movement modes

Three modes of ice movement were found. The first is a southward atmospherically forced movement into the Bering Sea requiring a $V_{40} > 11.5 \text{ ms}^{-1}$ to offset a preexisting **north-flowing** ocean current. The second mode is current-forced movement into the **Chukchi** Sea offsetting weak' opposing synoptic winds ($V_{40} \leq 7.5 \text{ ms}^{-1}$). The third mode is **usually large** ($>20 \text{ km [day]}^{-1}$) northward **ice** movement under **the** influence of southwest winds and a north-flowing ocean current.

b. Sea ice immobilization modes

There were two ice immobilization modes found in the Strait. The first is an apparent balance between wind stress from the north and a **current-** induced water stress from the south. Internal ice stresses and fast-ice boundary orientation must play a role, but they are not covered in this Study . This mode is short term, usually lasting less than one week. The second mode was found only 5 times in **11** years. **In** each case, the nomogram predicted large ice movement south through the Strait **when** there was none. Double, **solid** sea ice arches, made possible **by** the Diomed Islands anchoring

their middle column, were the apparent cause. A theoretical estimate of single-arch strength across the entire Bering Strait showed fracturing at the MAPN-calculated V_G 's. However, the same computation on double arches showed the ability to withstand the V_G 's generated during the arch periods. This longer-period immobilization mode (up to four weeks) can hinder spring whale migration into the Chukchi and aid in opening up the region. below the Strait as well as Norton Sound.

c. Driving force behind the mean north-flowing current in the Strait

Through the course of this study, examples of northward ice-flow movement events were seen without apparent southwesterly wind forcing and with large-scale atmospheric pressure fields conducive to raising the sea level in the Arctic Ocean (Chukchi) over that of the Bering. Also, northward ice movement continued three days beyond relaxation of strong northeasterly winds, precluding compensatory circulations due to local sea level differences.

This evidence implies that direct and indirect meteorological causes must be ruled out. Two recent theoretical papers have shed light on the possible causes for the northward-flowing current. The first is the work of Stigebrandt (1984), which cites global-scale salinity differences between the Atlantic and Pacific as a reason for mean northward flow of water through the Strait. The second is work by Liu and Leendertse (1985), which points to residual northward transport from the tide and ocean density (negligible in winter) fields.

d. Recommendations for future work

The MAPN-nomogram technique can be improved in several respects if a need arises. Bad predictions can often be traced to two major cases where a geostrophic balance does not exist. One case is under accelerating conditions when pressure is changing rapidly requiring an isallobaric component of the wind. Another case is when strong curvature of the isobars exists (radius of curvature less than 300 km), implying that a gradient wind balance is needed. The nomogram itself can be more finely tuned if more data of the type collected by Reynolds and Pease (1984) can be matched to satellite information. This data might prove very useful to determine further differences in northward ice movement driven by a wind and current push versus movement driven by a current alone. The MAPN accuracy can be improved by a cooperative visitation program involving the Russian sites in the network. A barometric standard could be used to calibrate all three sites to arrive at more precise V_p values from which V_G is calculated.

Acknowledgments. This study was funded by the Minerals Management Service, U.S. Department of the Interior, through interagency agreement with the National Oceanic and Atmospheric Administration, U.S. Department of Commerce, as part of the Outer Continental Shelf Environmental Assessment Program. The contract numbers were 83-ABC-00166 and 84-ABC-00107.

APPENDIX A

Comparison of Wind Stress (τ_a) and Water Stress (τ_w)

$$\tau_a = \rho_a C_a (U_a \cdot r_a)^2 \quad (A1)$$

$$\tau_w = \rho_w C_w U_w^2 \quad (A2)$$

where (using values typical of the Strait conditions)

$\rho_a \equiv$ density of dry air at $-20^\circ\text{C} \sim 1.4 \text{ kgm}^{-3}$

$C_a \equiv$ 10 m drag coefficient (Walter et al., 1984) for air/water " in the Bering Sea area $\sim 3 \times 10^{-3}$

$U_a \equiv$ average wind speed in the Zero Net Ice Motion Zone $\sim 10 \text{ ms}^{-1}$

$r_a \equiv$ ratio of surface wind speed (10 m) to the calculated geostrophic wind ~ 0.6 for arctic conditions. (Albright, 1980). Note: Albright used a high resolution surface pressure grid and multiyear data base to derive his r_a .

$\rho_w \equiv$ density of water at $0^\circ\text{C} \sim 1 \times 10^3 \text{ kgm}^{-3}$

$C_w \equiv$ 2 m drag coefficient for ice/water in the Bering Sea area $\sim 16 \times 10^{-3}$ (Pease and Overland, 1984)

$U_w \equiv$ typical current speed due only to tidal residuals in the Bering Strait area $\sim 0.1 \text{ ms}^{-1}$ (Liu and Leendertse, 1985).

This assumes that the usual sea surface slope downward to the north (Aagaard et al., 1985; Stigebrandt, 1984) driving the mean flow is all but eliminated by a V_{40} of 1.0 ms^{-1} .

After inserting the above values in (A1) and (A2):

$$\tau_a = 0.15 \text{ Nm}^{-2}; \quad \tau_w = 0.16 \text{ Nm}^{-2}$$

APPENDIX B

Estimating Arch Strengths

The theory predicting the limiting spans for arching of granular material flowing through a chute (Gardner, 1962; Richmond and Gardner, 1962) as adapted by Sodhi (1977) will be used to show the reason for double arch existence despite the strong MAPN winds. It seems possible that the double arches are a natural phenomenon resulting from a period of strong wind velocities that would destroy a single arch across the entire Strait. Figure 12 is an enlargement of the Strait area from Fig. 10 with the Chukchi and Seward Peninsulas and the Diomede Islands again shown as anchor points for the sea ice. The dashed curves differentiate the sea ice arches from the e - - - coastal boundaries and the large, dark area is open water.. The single-arch strength can be estimated by comparing the arches in Fig. 12 to the inset drawing. The span width (2A) of the arch from the Diomede Islands to the Seward Peninsula is 43 km and from the Chukchi Peninsula to the Diomedes is 37 km. The width of the Diomede Island blockage zone (see Shapiro and Burns, 1975a) is 7 km. Theta (θ) can be read with a compass from Fig. 12. The eastern arch (Diomede Islands-Seward Peninsula) has a $\theta \sim 30^\circ$ while the western arch (Diomede Islands-Chukchi Peninsula) is more irregular with an average θ of $\sim 80^\circ$ also. From (B1)

$$\theta = n/4 + \phi/2 \quad (\text{see inset Fig. 12}) \quad (\text{B1})$$

where $\phi \equiv$ angle of internal friction

ϕ is estimated as 70° for both arches. Next (B2) is used to solve for τ as defined by (B3) (Sodhi, 1977).

$$\lambda = \frac{c}{\tau} (1 + \sin \phi) \quad (\text{B2})$$

$$\tau = \rho C V^2 \quad (\text{B3})$$

Here:

$\lambda \equiv$ half span width (m)

$c \equiv$ cohesive strength (Nm^{-1})

$\tau \equiv$ net stress per unit area (Nm^{-2})

(wind and water stress combined)

$\rho \equiv$ mass density of medium (kg m^{-3})

$C \equiv$ drag coefficient (unitless)

$V \equiv$ wind velocity (ms^{-1})

Cohesive strength (c) for Amundsen Channel (Beaufort Sea, June) sea ice in a solid arch was estimated from (B2) and (B3) at failure to be 1993 Nm^{-1} . (Sodhi, 1977). The net stress (τ) applied to this arch (zero water stress assumed) was calculated using a typical 10-m air-ice drag coefficient (C) of 1×10^{-3} and local winds for V . Recent Bering Sea work (Walter et al., 1984) shows C to be 3×10^{-3} or three times the Sodhi (1977) estimate. Using this newer value for C would give $c = 5979 \text{ Nm}^{-1}$ as the cohesive strength of sea ice at failure. Given this c , taking $\phi = 70^\circ$, and $\lambda \sim 20 \times 10^3 \text{ m}$ (double arches) and substituting into (B2), τ (net) = 0.58 Nm^{-2} .

Remembering that water stress generally opposes wind stress from the north, τ_w is defined by (A2) and estimated to be -0.16 Nm^{-2} . The net stress τ , as seen in (B4) will allow calculation of air stress τ_a defined by (A1):

$$\tau = \tau_a + \tau_w \quad (\text{B4})$$

Therefore $\tau_a = (0.58) - (-0.16) = 0.74 \text{ Nm}^{-2}$.

Hence from (A1)

$$U_a = 23 \text{ ms}^{-1} = V_{40} \text{ on the nomogram axis.}$$

This geostrophic wind corresponds to a surface wind of 13.8 ms^{-1} (Albright, 1980). Surface winds of this magnitude occur less than 10% of the time (Brewer et al., 1977) at Tin City (near Cape Wales, Fig. 1). The estimated V_{40} value of 23 ms^{-1} is close to the maximum V_{40} of 26 ms^{-1} -calculated for three of the arch cases. The cohesive-strength estimate used here could have been slightly larger since no evidence of arch breakup during the these winds existed. The observed manner of arch destruction is a relaxation of the northerly winds and a switch to pure water stress or combined wind and water stress from the south. It should be noted that using the half-span length for a single arch across the entire Strait ($\sim 42.5 \text{ km}$) in (B2) with all other parameters the same yields $\tau = 0.27 \text{ Nm}^{-2}$. Insertion into (B4) gives a $V_{40} = 17.5 \text{ ms}^{-1}$ which would be exceeded by 50% of the MAPN velocities during arch occurrence, thereby leading to arch failure.

REFERENCES

- Aagaard, K., A. T. Roach, and J. D. Schumacher, 1985: On the wind-driven variability of the flow through the Bering Strait. J. Geophys. Res., 90, 7213-7221.
- Agerton, D. J., and J. R. Kreider, 1979: Correlation of storms and major ice movements in the nearshore Alaska Beaufort Sea. Fifth International Conference on Port and Ocean Engineering under Arctic Conditions. Norwegian Institute of Technology, 1, 177-189. (Available from the University of Trondheim, N7034 Trondheim-NTH, Trondheim, Norway).
- Albright, M., 1980: Geostrophic wind calculations for AIDJEX, in Sea Ice Processes and Models, edited by Robert S. Pritchard, University of Washington Press, Seattle, 402-409. (Available from University of Washington Press, Box 85569, Seattle, WA 98145.)
- Brewer, W. A., H. F. Diaz, A. S. Prechtel, H. W. Searby and J. L. Wise, 1977: Climatic Atlas of the Outer Continental Shelf Waters and Coastal Regions of Alaska. NOAA, NCC, EDS, Asheville, 409 pp. (Available from the National Climatic Center, Asheville, NC 28801-2696.)
- Browning, K. A., 1982: Preface in Nowcasting (cd. by K. A. Browning). Academic Press, New York, IX-XI.
- Brunt, D., 1941: Physical and Dynamical Meteorology. Cambridge University Press, London, 428 pp.
- Coachman, L. K., and K. Aagaard, 1981: Reevaluation of water transports in the vicinity of Bering Strait, Chapter 7 in The Eastern Bering Sea Shelf: Oceanography and Resources (cd. by D. W. Hood and J. A. Calder), University of Washington Press, Seattle, 95-110. (Available from University of Washington Press, Box 85569, Seattle, WA 98145.)

Coachman, L. K., K. Aagaard and R. B. Tripp, 1975: Bering Strait: The Regional Physical Oceanography. University of Washington Press, Seattle and London, 172 pp. (Available from the University of Washington Press, Box 85569, Seattle, WA 98145.)

Dickey, W. W., 1961: A study of a topographic effect on wind in the arctic. J. Meteor. , 18, 790-803.

Gardner, G. C., 1962: Limiting conditions for flow of a cohesive granular material down an inclined plane (chute) or between parallel inclined walls (bin or channel). Chem. Eng. Sci., 17,107-1086. (Available from Chemical Engineering Science Journal, Pergamom Press, Inc., Journals Division, Maxwell House, Maxwell House, Fairview Park, Elmsford, NY 10523.)

Holton, J. R., 1973: An Introduction to Dynamic Meteorology. Academic Press, New York, 319 pp.

Hufford, G., and R. Scheidt, 1984: Interaction of Norton Sound Ice and Weather, Abs. in 1984 Arctic Science Conference (35th Alaskan Conference), Oct. 2-5, 1984, Anchorage, Alaska, sponsored by Amer. Assn. for Adv. of Sci. - Arctic Div., Amer. Met. Sot. and Arctic Inst. of North America, 109 pp.

Kovacs, A., and D. S. Sodhi, 1981: Sea ice piling at Fairway Rock, Bering Strait, Alaska: Observations and theoretical analyses. Proc. Sixth Int. Conf. on Port and Ocean Eng. under Arctic Cond. POAC-81, Quebec, Canada, 2, 985-999. (Available from the Dept. of Civil Engineering, Univ. Laval, Quebec, Canada G1K 7P4.)

Kovacs, A., D. S. Sodhi and G.F.N. Cox, 1982: Bering Strait sea ice and the Fairway Rock icefoot. Cold Regions Res. and Engineering Laboratory, CRREL Rpt. 82-31, Hanover, NH, 40 pp. (Available from CRREL, 72 Lyme Rd. , Hanover, NH 03755-1290.)

- Kozo, T. L., 1984: Mesoscale wind phenomena along the Alaska Beaufort Sea Coast, in The Alaska Beaufort Sea: Ecosystems and Environment (ed. by P. W. Barnes, D. M. Schell and E. Reimnitz). Academic Press, New York, pp. 23-45.
- , 1982: An observational study of sea breezes along the Alaska Beaufort Sea Coast: Part I. J. App. Meteor. , 12, 891-905.
- , 1980: Mountain barrier baroclinity effects on surface winds along the Alaskan Arctic Coast. Geophysical Research Letters, 7, 377-380.
- and W. B. Tucker, 1974: Sea ice bottomside features in the Denmark Strait. J. Geophys. Res., 79, 4505-4511.
- Liu, S. K., and J. J. Leenderste, 1985: Modeling the Alaskan coastal waters, Rand Rept. R-3236-NOM 85. (Available from the Rand Corporation, Santa Monica, CA, and National Ocean Service, Anchorage, Alaska.)
- Pease, C. H., and J. E. Overland, 1984: An atmospherically driven sea-ice drift model for the Bering Sea. AM. Glaciol. , 5, 111-113.
- Ray, V. M., and W. R. Dupre, 1981: The ice-dominated regimen of Norton Sound and adjacent areas of the Bering Sea. Chapter 16 in The Eastern Bering Sea Shelf: Oceanography and Resources (ed. by D. W. Hood and J. A. Calder). University of Washington Press, Seattle, pp. 263-178. (Available from University of Washington Press, Box 85569, Seattle, WA 98145.)
- Reimer, R. W., R. S. Pritchard and M. D. Coon, 1979: Beaufort and Chukchi Sea ice motion: Part 2. Onset of large scale Chukchi Sea ice breakout, Flow Res. Rpt. No. 133, Kent, Washington, 92 pp. (Available from Flow Industry, Inc., 21414 68th Ave. So., Kent, WA 98032.)

- Reynolds, M., and C. H. Pease, 1984: Drift characteristics of the northeastern Bering sea ice during 1982. NOAA Tech. Memo. ERL-PMEL-55, Seattle, Washington, 135 pp. (Available as PB 84-213982 from the Natl. Tech Inf. Serv., Springfield, VA.)
- Richmond, O., and G. C. Gardner, 1962: Limiting spans for arching of bulk material in vertical channels. Chem. Eng. Sci., 17, 1071-1078. (Available from Chem. Eng. Sci. Journal, Pergamon Press, Inc., Journals Div. , Maxwell House, Fairview Park, Elmsford, NY 10523.)
- Shapiro, L. H., and J. J. Burns, 1975a: Major late-winter features of ice in Northern Bering and Chukchi Seas as determined from satellite imagery. Geophysical Inst. Rpt. No UAG R-236, Sea Grant Rpt. No. 75-8, University of Alaska, Fairbanks, 14 pp. (Available from Geophysical Institute, University of Alaska, Fairbanks, AK 99775.)
- Shapiro, L. H., and J. J. Burns; 1975b: Satellite observations of sea ice movement in the Bering Strait region. In Climate of the Arctic, University of Alaska, Fairbanks, pp. 379-386. (Available from the Geophysical Institute, University of Alaska, Fairbanks, AK 99775.)
- Sodhi, D. S., 1977: Ice arching and the drift of pack ice through restricted channels. Cold Regions Research and Engineering Laboratory, CRREL Rpt. 77-18, Hanover, New Hampshire, 11 pp. (Available from CRREL, 72 Lyme Rd. , Hanover, NH 03755-1290.)
- Stigebrandt, A., 1984: The North Pacific: a global-scale estuary. J. Phys. Oceanogr. , 14, 464-470.
- Stringer, W. J., and G. L. Hufford, 1982: Interaction of Bering Sea and Norton Sound pack ice. Arctic and Alpine Res., 14,149-156.
- Walter, B. A., J. E. Overland and R. O. Gilmer, 1984: Air-ice drag coefficients for first-year sea ice derived from aircraft measurements. J. Geophys. Res., 89, 6525-6531.

TABLE 1. Selected net sea ice movement (I) events for the Bering Strait plotted in Fig. 4.

Mode 1. Into Bering Sea (wind-forced), winds opposed to normal ocean current direction.

a. $I > 20 \text{ km (day)}^{-1}$ Zone ($V_{40} > 16.5 \text{ ms}^{-1}$)

Events: Y(14,15 Apr 82), 2(14,15 Mar 82)

γ(17 Feb 81), A(17 Jan 83), Δ(11 Feb 84)

φ(6,7 Mar 78), ψ(27 Dec 76)

b. $I < 20 \text{ km (day)}^{-1}$ Zone, ($11.5 \text{ ins}^{-1} < V_{40} \leq 16.5 \text{ ms}^{-1}$)

Events: U(18 Feb 84), X(19 Feb 83), N(11 May 81)

V(22 Feb 76), W(27 Feb 79), M(2 May 77)

Mode 2. Into Chukchi Sea (ocean current forced, weak winds oppose current direction).

a. $I < 20 \text{ km (day)}^{-1}$ Zone, ($0 \text{ ins}^{-1} < V_{40} \leq 7.5 \text{ ms}^{-1}$),

Events: K(9 Apr 82), R(7 Dec 76), T(3 May 84)

Q(25 Feb 79), 1(23 Jan 82), Σ(21 Mar 78)

Mode 3. Into Chukchi Sea (major forces are ocean current and wind in the same direction)

a. $I > 20 \text{ km (day)}^{-1}$ Zone, ($V_{40} \leq 0 \text{ ms}^{-1}$), see Definition B below for direction.

Events: G(8 Apr 82), θ(6 Feb 82), 11(4 Feb 82),

ρ(22 Mar 78), □(31 Jan 81), w(24 Feb 82)

∧(10,11 Feb 79), B(16,17 Feb 79), C(1,2 Feb 76)

D(27,28 Feb 76), E(5 May 84), F(2,3 Mar 82)

TABLE 1. (continued)

Mode 4. **First** immobilization mode, ocean current and wind in opposition (respective stresses apparently **in** balance)

a. Zero Net Ice Movement Zone ($I = 0$)

$$(7.5 \text{ ms}^{-1} < V_{40} \leq 11.5 \text{ ms}^{-1})$$

Events: J(25 Mar 82), S(21 Feb 76), H(24 Jan 83)

L(21 Apr 81), O(11 Apr 78), P(2 Apr 78)

Definitions:

A. $v_{40} \equiv V_G$ speed component parallel to Strait axis 40°E from north (Fig. 4).

B. If V_G direction $\sim 310^\circ$ or $< 130^\circ$
 $= 310^\circ$ or $= 130^\circ$ $\rightarrow v_{40} = 0$
 $130^\circ < V_G < 310^\circ$ $\rightarrow v_{40} < 0$

TABLE 2. Net buoy displacements (X) versus nomogram predictions (NP).

Date (82)	Buoy #	x (km, N or S)	\bar{v}_G (direction ["from"], speed [ms^{-1}])	NP(km)	Agreement
3 Feb	2324	39N	139, 11	>20N	yes
4 Feb	2324	39N	195, 11	>20N	yes
5 Feb	2324	12N*(some west motion)	112, 17	<20N	yes*
6 Feb	2320, 2323, 2324	44N (Ave.)	226, 16	>20N	yes
7 Feb	2320, 2323 2324	72N (Ave.)	213, 16	>20N	yes
8 Feb	2320, 2323	66N (Ave.)	231, 9	>20N	yes
9 Feb	2325	16N	3 2 0 , 4	<20N	yes
10 Feb	2325	10N	057, 7	<20N	yes
11 Feb	2325	22N	011, 3 *(in 3 ms^{-1} zone consider ~ 0)	>20N	yes*
12 Feb	2325	36N	* $\sim 180^\circ$ direction change in 12 h	no prediction	-**
Feb	2325	10s	075, 16	<20S	yes
14 Feb	2325	65S	021, 17	>20S	yes
15 Feb	2323, 2325	74S (Ave.)	017, 17	>20S	yes
16 Feb	2320, 2324	77S (Ave.)	025, 18	>20S	yes
17 Feb	2320, 2324	45S (Ave.)	037, 13	<20S	no

TABLE 2. (continued)

Date (82)	Buoy #	x (km, N or S)	\bar{V}_G (direction[°from]), speed [ms^{-1}])	NP(km)	Agreement
18 Feb	2324	44s	024, 13	<20S	no
24 Feb	2320,2324	45N (Ave.)	205, 14	>20N	yes
25 Feb	2320,2324	27N (Ave.)	195, 8	>20N	yes
26 Feb	2320,2324	76N (Ave.)	193, 10 "	>20N	yes
27 Feb	2324	12N	251, 6	>20N	no
5 Mar	2325	36N	152, 11	>20N	yes
6 Mar	2325	45N	125, 18	>20N	yes
7 Mar	2325	45N	140, 15	>20N	yes
8 Mar	2325	78N	137, 24	>20N "	yes
9 Mar	2325	65N	168, 13	>20N	yes
19 Mar	2325	24S	057, 23	>20S	yes
20 Mar	2325	5 1S	053, 29	>20S	yes
21 Mar	2325	36S	062, 23	>20S	yes
22 Mar	2325	8S	045, 21 *(P increased ~8 mb in 12 h at all 3 stations)	. 20s	no*
23 Mar	2325	5N (some east motion)	339, 4	<20N	yes*
24 Mar	2325	~3N (some east motion)	002, 8	net zero N-S motion	yes*
25 Mar	2325	~3N (some east motion)	039, 8	net zero N-S motion	yes*

TABLE 2. (continued)

Date (82)	Buoy #	x (km, N or S)	\bar{V}_G (direction[°from]), speed [ms^{-1}])	NP(km)	Agreement
26 Mar	2325	11N	135, 10*(borderline)	>20N	--*
27 Mar	2325	23N	133, 13	>20N	yes
28 Mar	2325	22N	123, 5	>20N	yes
29 Mar	2325	8N	049, 10 *(P increased " ~5 mb in 12 h at all stations)	zero net motion	no*
30 Mar	2325	8N	036, 9	zero net motion	no
31 Mar	2325	~2N	062, 6	<20N	yes
1 Apr	2325	7N	008, 6	<20N	yes
2 Apr	2325	47N	163, 9	>20N	yes
3 Apr	2325	36N	216, 16	> 20N	y e s

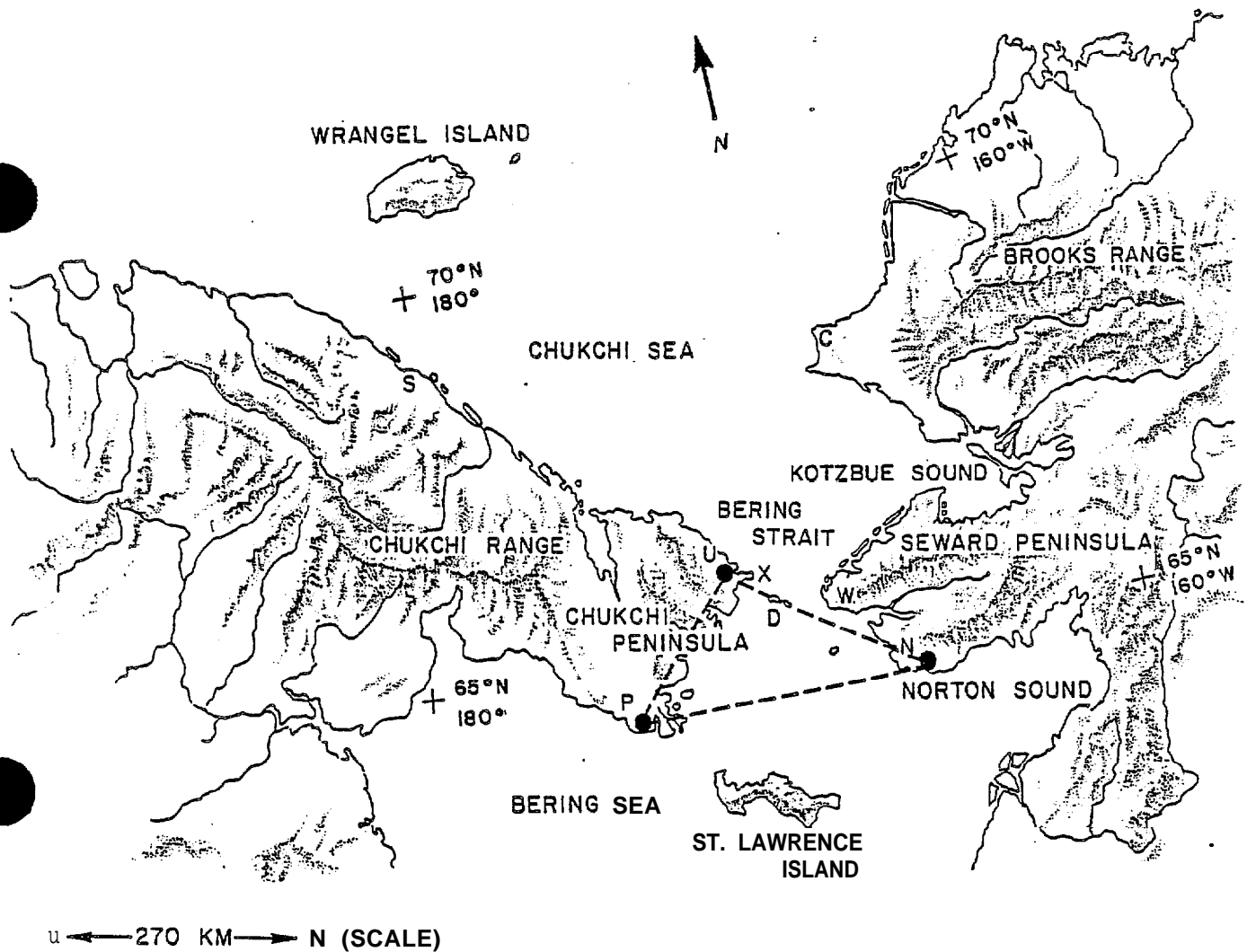


Fig. 1. The surface pressure station network P-U-N (dashed triangle) covering the Bering Strait region. P is Bukhta Provideniya, U is Uelen (both in Siberia) and N is Nome, Alaska. The Diomedede Islands (D) are in the center of the Strait, Cape Schmidt (S) is below Wrangel Island, Cape Lisburne (C) is north of Kotzebue Sound, and Cape Wales (W) and Cape Dezhneva (X) are on the tips of the Seward and Chukchi Peninsulas respectively. Mountain axes are shaded for emphasis.

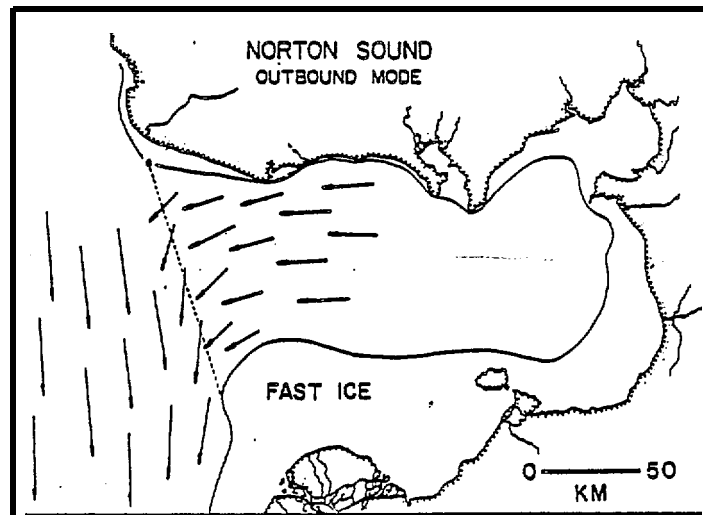
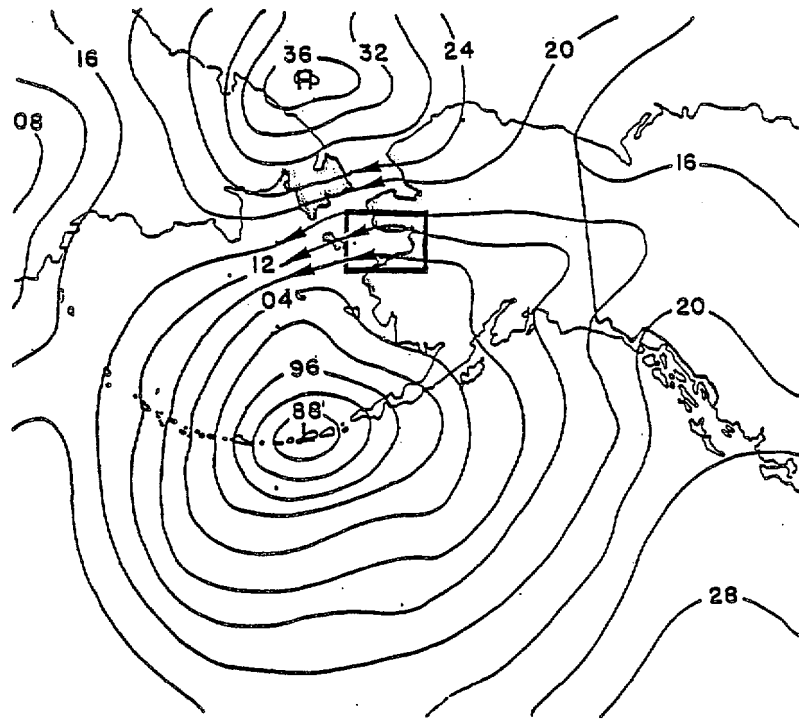


Fig. 2. The atmospheric pressure field (top) that is associated (Hufford and Scheidt, 1984) with ice movement (bottom) southward below the Strait and westward out of Norton Sound (Stringer and Hufford, 1982). Arrows on isobars (top) indicate wind direction in the Strait area. For isobar values (rob) less than 60 add 1000 mb, if greater than 60 add 900 mb. Fast ice edge is within solid line (bottom)].

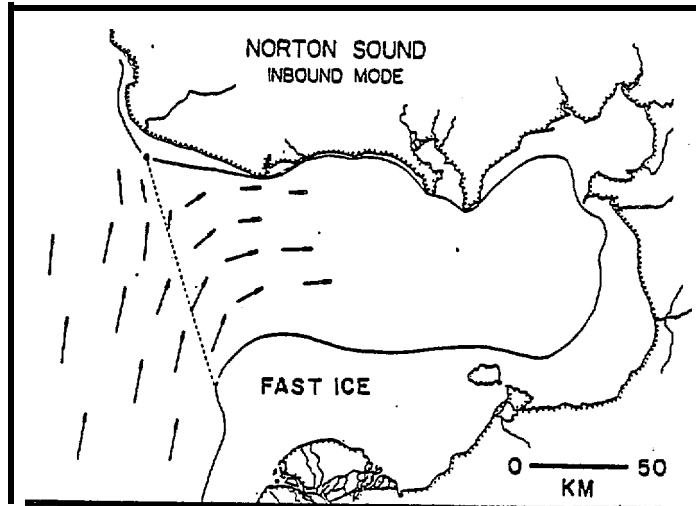
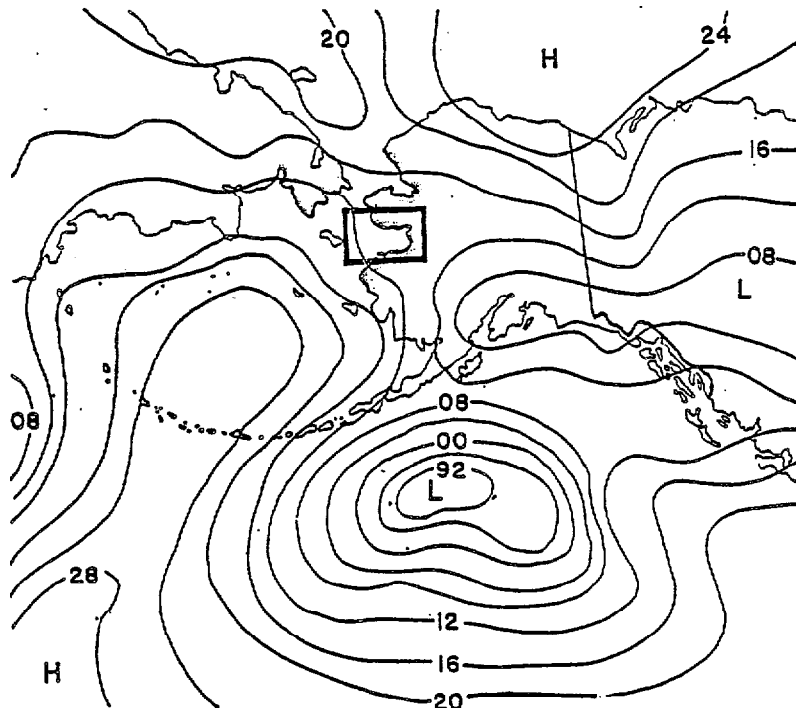


Fig. 3. The "relaxed" atmospheric pressure field (top) associated (Hufford and Scheidt, 1984) with ice movement northward (bottom) into the Strait and eastward into Norton Sound (Stringer and Hufford, 1982.) For isobar values (rob) less than 60, add 1000 mb, if greater than 60 add 900 mb. Fast ice edge is within solid line (bottom).

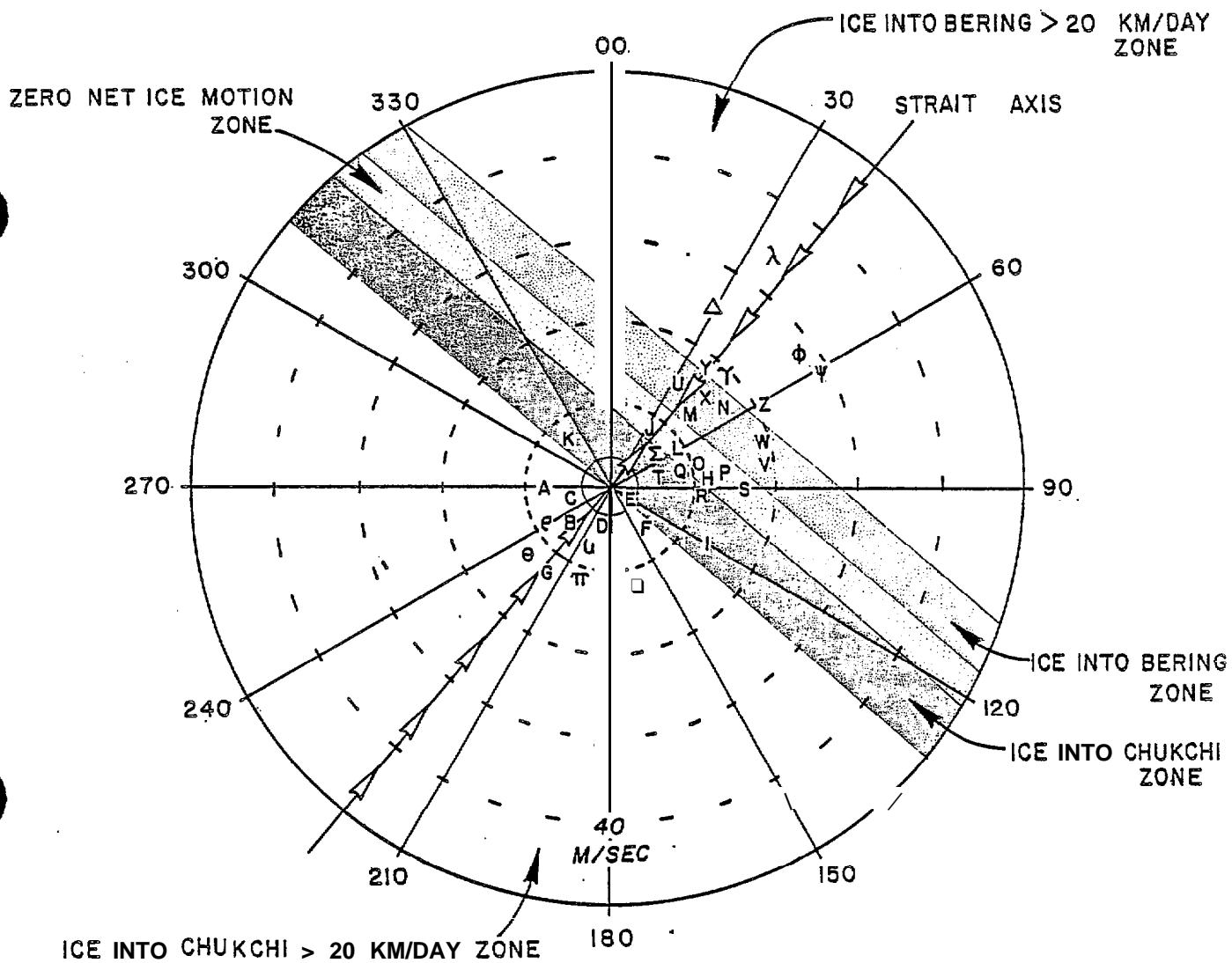


Fig. 4. The Bering Strait sea ice movement prediction nomogram with Greek and Latin letters representing sample MAPN-computed V_G 's used in its construction (see Table 1). The Strait axis is 40" from the north and has ice movement arrows meeting in the Zero Net Ice Motion Zone. The center solid-line circle is the $\leq 3 \text{ ms}^{-1}$ wind-speed zone and it represents direction uncertainties $>15^\circ$.

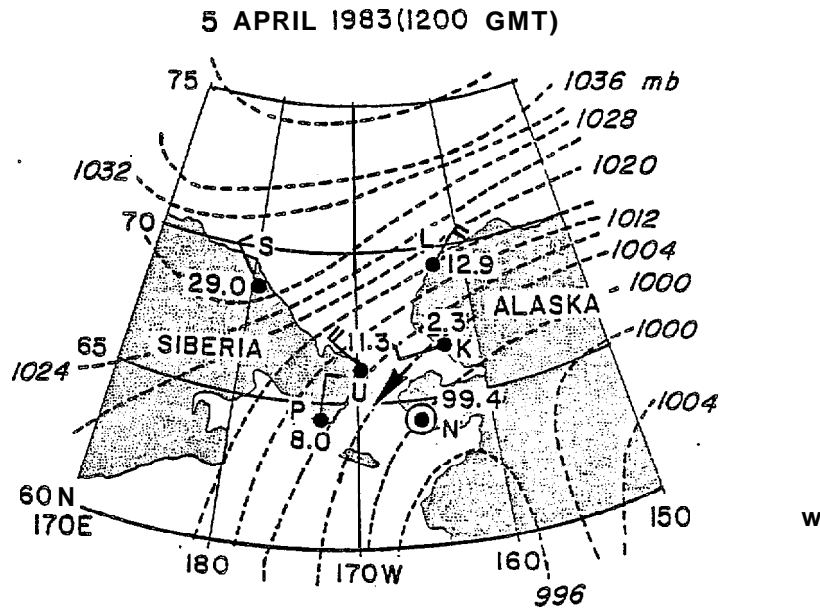


Fig. 5. Orographic effects on surface wind velocities despite a well defined isobaric pattern (dashed lines). The numbers adjacent to sites are surface pressures in mb minus 1000, unless the number is greater than 60, then pressures are in mb minus 900. Surface wind speeds are $\sim 5 \text{ ms}^{-1}$ for each perpendicular flag, $\sim 2.5 \text{ ms}^{-1}$ for slant flags (i.e., K), and ~ 0 for a circle (i.e., N). The stations shown are Provideniya [P], Uelen [U], Nome [N], Kotzebue [K], Point Lay [L], and Cape Schmidt [S]. The MAPN-computed V_G direction is shown by the arrow.

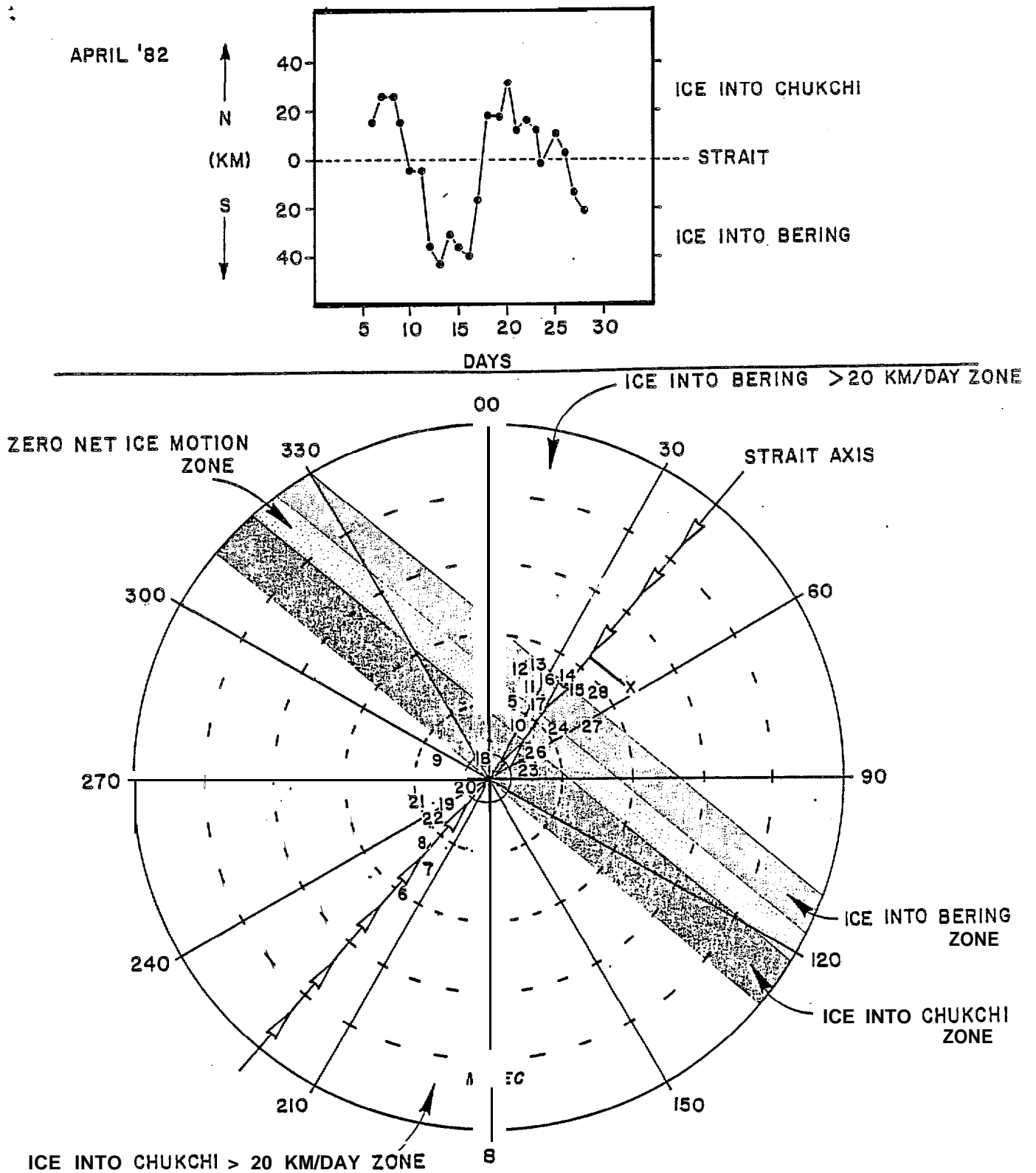


Fig. 6. Satellite imagery derived ice displacement (top) compared to MAPN V_G 's for 6-28 April 1982 plotted with corresponding day numbers on the sea ice movement prediction nomogram (bottom). The number positions represent wind velocity vectors whose V_{40} components define the daily predicted ice movement zone. X is a sample V_G calculated from surface pressure data in Fig. 5. Drawing a perpendicular line from X to the Strait axis results in a $V_{40} = 2.2 \text{ m s}^{-1}$. This is the Ice Into Bering >20 km (day)⁻¹ Zone.

21 APRIL 1982 (1200 GMT)

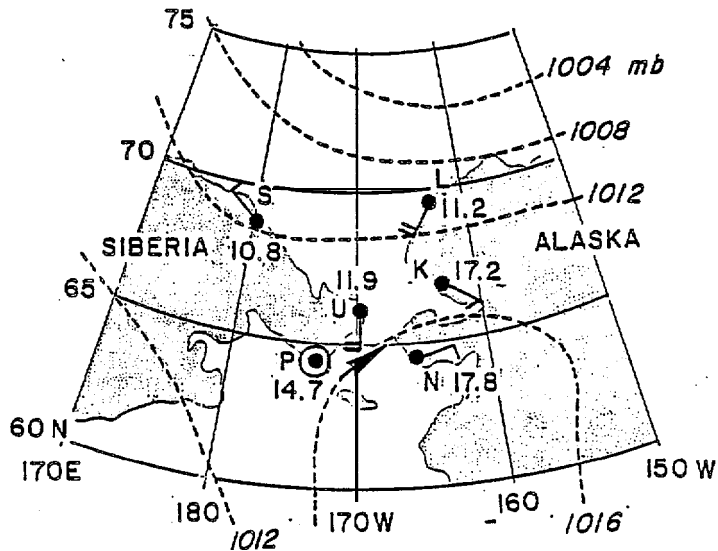


Fig. 7. An example of the lack of detail on an NMC surface isobaric analysis. The station, surface pressure, flag, and V_G designations are as in Fig. 5.

25 MARCH 1978 (1200 GMT)

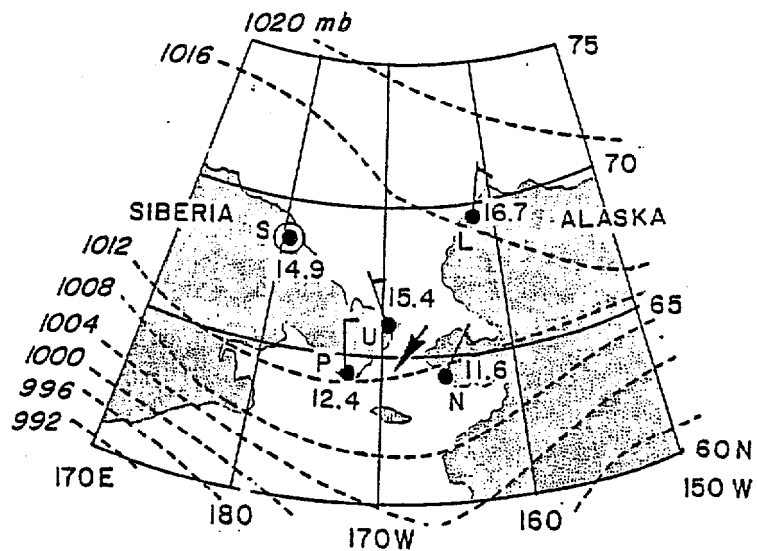


Fig. 8. An example of the advantages of the MAPN analysis over both pattern recognition and NMC surface isobaric analysis. The station, surface pressure, flag, and V_G designations are as in

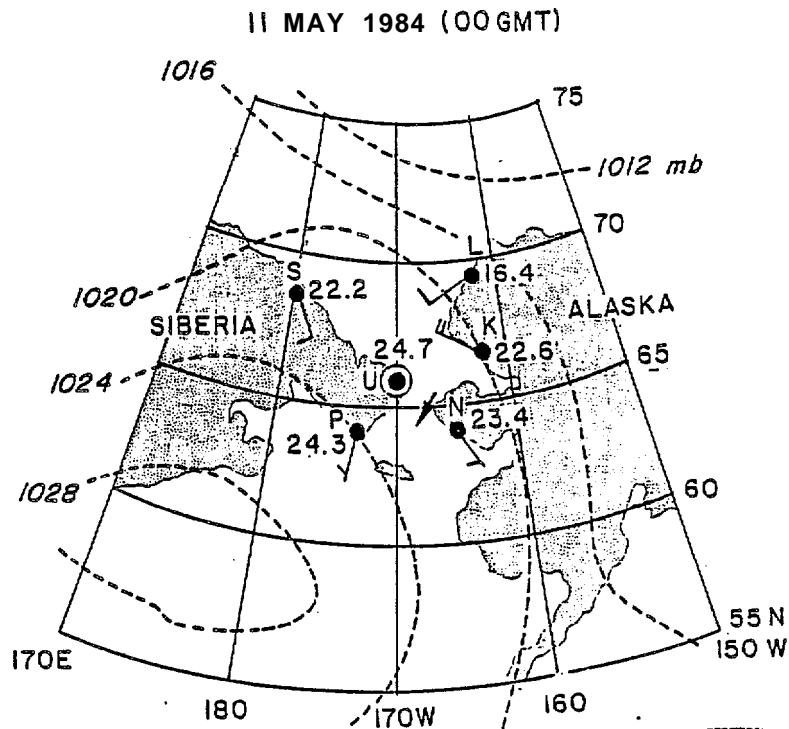


Fig. 9. A section of an NMC surface pressure analysis that indicates weak surface winds and no apparent meteorological reasons for sea level in the Bering to be higher than that of the Chukchi. Station, flags, and isobars are indicated as "in Fig. 5.

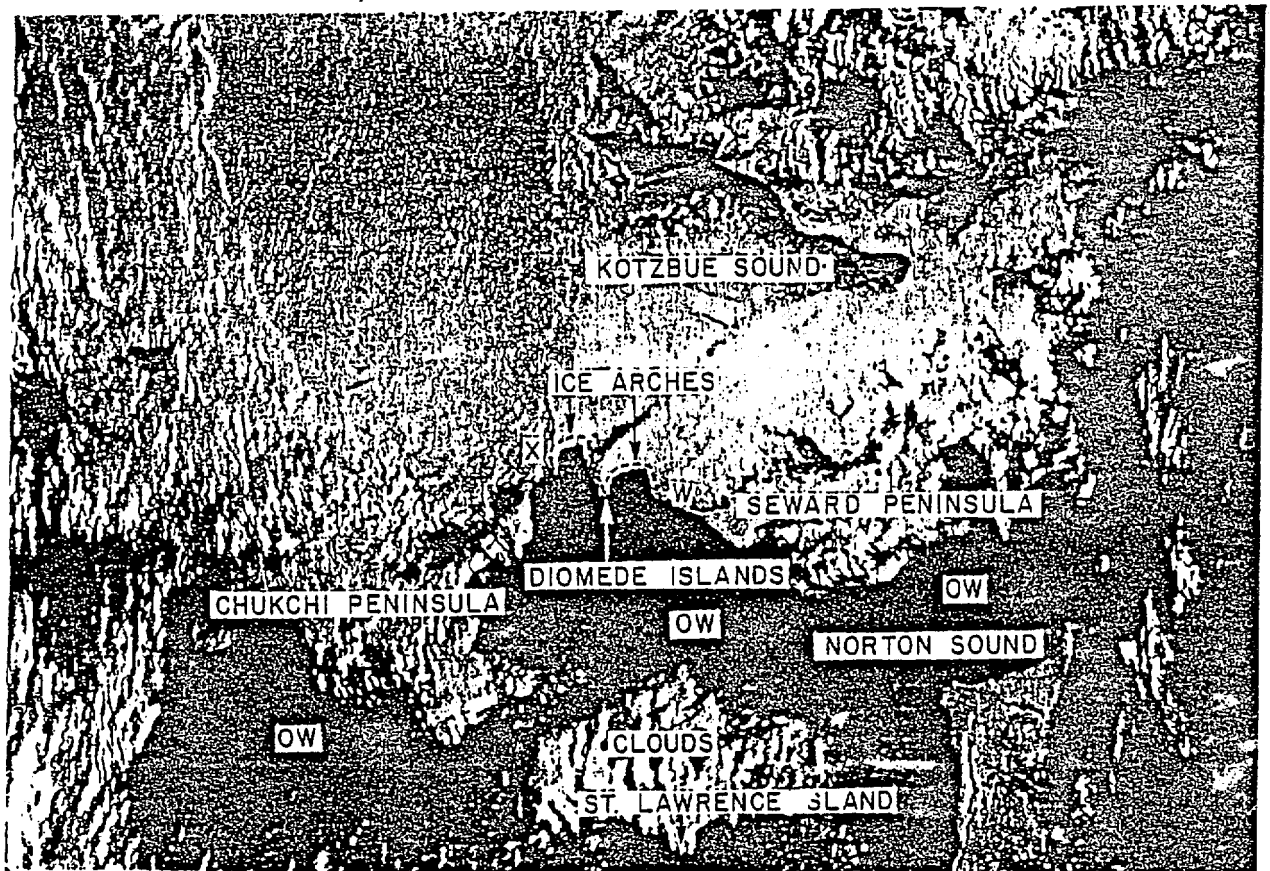


Fig. 10. A photograph made from a satellite image taken 5 May 1980 showing a solid, double ice arch in the Bering Strait.

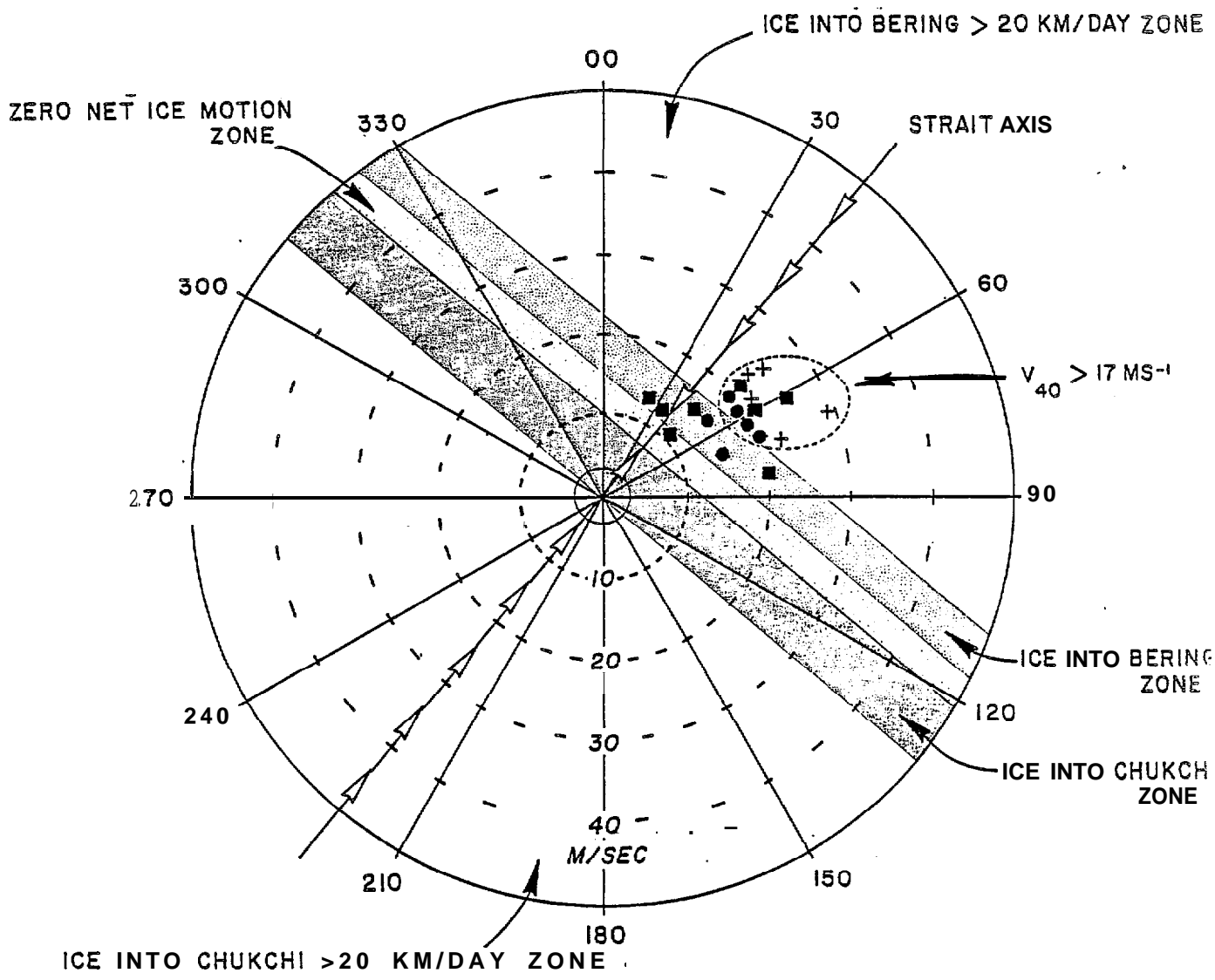


Fig. 11. Samples of MAPN V_G 's from designated double-arch periods 14 April - 10 May 1980 (\cdot), 26 February - 8 March 1984 ($+$), and 22 March - 21 April 1984 (\square) plotted on the nomogram. There are **several** cases (enclosed by dashed oval) with $V_{40} \geq 17 \text{ ms}^{-1}$ indicating a predicted ice movement into the Bering Sea of greater than $20 \text{ km}(\text{day})^{-1}$.

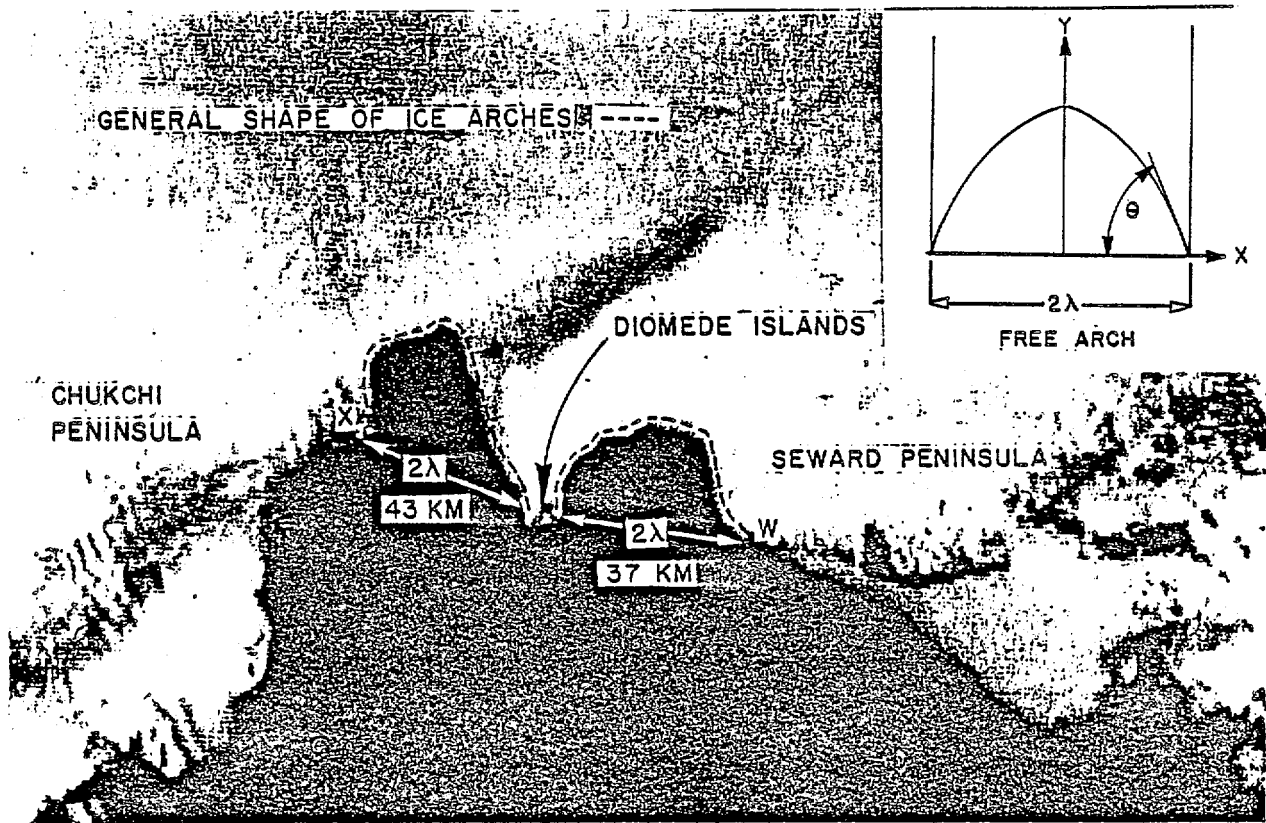


Fig. 12. An enlargement of the Strait area taken from the Fig. 10 photograph. The dashed curves show the actual sea ice arches to avoid confusion with land boundaries. The inset (top) is a sketch of an idealized free arch showing the span width (2λ) and the angle (θ) between the horizontal and tangent to the free surface.